Short-term Mechanical Strength Prediction of Ultra-High Performance Concrete using Noncontact Synthetic Aperture Radar Imaging

Tzuyang Yu, Arkabrata Sinha, Jianqiang Wei, Ronan Bates, Tek Dhant, and Harsh Gandhi
Department of Civil and Environmental Engineering
University of Massachusetts Lowell
One University Avenue, Lowell, MA 01854, U.S.A.

ABSTRACT

In recent decades, the use of ultra-high performance concrete (UHPC) has been widely accepted by the construction industry for buildings and bridges. The exceptional properties of UHPC on strength (18 ksi 35 ksi) and durability (freeze-thaw resistance, abrasion resistance, chloride ion penetration resistance) have made it a popular construction material for durable and sustainable civil infrastructure systems. The objective of this paper is to investigate the shortterm mechanical strength development of UHPC specimens using a noncontact synthetic aperture radar (SAR) imaging sensor. UHPC cubes and cylinders were designed and manufactured for nondestructive strength monitoring and kinematic and rheological characterization. Change in moisture content and distribution inside UHPC cylinders was monitored by a laboratory 10-GHz SAR imaging sensor inside a microwave anechoic chamber at UMass Lowell. Hydraulic permeability of UHPC specimens was measured by their bulk electrical resistivity using a concrete resistivity meter (ASTM C1876). The rate of water uptake (absorption or sorptivity) was characterized by an apparatus used to measure the water absorption rate of both the concrete surface and interior concrete (ASTM C1585). Early stage shrinkage behavior of UHPC specimens during the first seven days was also measured using a shrinkage cone. Level of cement hydration in UHPC specimens was quantified by the loss of free water inside UHPC and remotely measured by the SAR imaging sensor. Mechanical strength development in UHPC specimens was monitored by following ASTM C109/C109M. From our preliminary result, it is found that change in SAR amplitude and amplitude distribution can be correlated to the level of strength development.

Keywords: Moisture content, concrete, water-to-cement ratio, synthetic aperture radar, remote sensing, K-R-I transform

1. INTRODUCTION

Portland cement concrete (PCC) is the most widely used artificial and engineering material in the history of mankind. While most PCC structures can be designed to provide their service for 50 years to 75 years (e.g., highway bridges), other design factors such as sustainability have been gradually driving the development of novel PCC products, such as self-consolidating concrete, green concrete, self-healing concrete, ultra-high strength concrete (UHSC) and ultra-high performance concrete (UHPC). In recent decades, the use of UHPC has been widely accepted by the construction industry for buildings and bridges. The exceptional properties of UHPC on strength (18 ksi 35 ksi) and durability (freeze-thaw resistancefreezing-and-thawing,, 1-3 abrasion resistance, chloride ion penetration resistance⁴) have made it a popular construction material for durable and sustainable civil infrastructure systems. These features of UHPC represent not only superior performance over traditional PCC but also significantly reduced maintenance and lifecycle costs to municipals and state DOTs (Department of Transportation).

The objective of this paper is to investigate the short-term mechanical strength development of UHPC specimens using a noncontact synthetic aperture radar (SAR) imaging sensor. UHPC cubes and cylinders were

Further author information: (Send correspondence to T. Yu) E-mail: tzuyang_yu@UML.EDU, Telephone: 1 978 934 2288

designed and manufactured for nondestructive strength monitoring and kinematic and rheological characterization. Change in moisture content and distribution inside UHPC cylinders was monitored by a laboratory 10-GHz SAR imaging sensor inside a microwave anechoic chamber at UMass Lowell. Hydraulic permeability of UHPC specimens was measured by their bulk electrical resistivity using a concrete resistivity meter (ASTM C1876). The rate of water uptake (absorption or sorptivity) was characterized by an apparatus used to measure the water absorption rate of both the concrete surface and interior concrete (ASTM C1585). Early stage shrinkage behavior of UHPC specimens during the first seven days was also measured using a shrinkage cone. Level of cement hydration in UHPC specimens was quantified by the loss of free water inside UHPC and remotely measured by the SAR imaging sensor. Mechanical strength development in UHPC specimens was monitored by following ASTM C109/C109M.

In this paper, our research approach is first introduced, followed by the experimental program on specimen preparation and laboratory SAR imaging. Results and discussion are summarized. Conclusions are finally presented.

2. SYNTHETIC APERTURE RADAR IMAGING

Synthetic aperture radar (SAR) imaging is a remote sensing technique capable of producing surface and subsurface profile for dielectric targets like UHPC. With multiple imaging modes (spotlight, stripmap, and inverse), flexible resolutions (synthetic aperture) and bandwidth enhancement, SAR imaging has demonstrated its promising potential for detecting subsurface delamination, determination of the water-to-cement ratio, estimation of chloride content, characterization of moisture content of concrete.^{5–7}

The fundamental principal of SAR imaging for subsurface sensing in civil engineering is electromagnetic (EM) scattering in dielectric media. Propagation and scattering of EM waves in free space can be generated/received by a radar system for non-contact inspection of materials and assessment of structures. Since concrete is the most widely used engineering material in the world, the ability of EM waves traveling in free space (air) and inside concrete is a superior property over other techniques such as optical and acoustic/ultrasonic methods. In SAR imaging, reflected EM waves in time domain are first transformed to frequency domain via one-dimensional (1-D) Fourier transform. The us of backprojection algorithms allows us to generate 1-D sub-images for superposition. When a greater synthetic aperture is used, more sub-images can be produced and used in image superposition. Consequently, final SAR images with better resolutions can be obtained. Formulation of SAR imaging used in this paper can be found in the literature.

In this paper, quantification of SAR images is achieved by using two SAR image parameters; maximum SAR amplitude I_{max} and integrated SAR amplitude I_{int} . Their definitions are provided in the following.

$$I_{max} = \max\{I(r, r_x)\}\tag{1}$$

where $I(r, r_x)$ is a matrix containing SAR amplitude at any given coordinate (r, r_x) .

$$I_{int} = \int_{r_1}^{r_2} \int_{r_{x_1}}^{r_{x_2}} I(r, r_x) dr dr_x$$
 (2)

where r_1 and r_2 are the range coordinates (lower bound and upper bound) used in the windowing of SAR images for calculating I_{int} and r_{x1} and r_{x2} the cross-range coordinates (lower bound and upper bound).

3. EXPERIMENTAL PROGRAM

3.1 Materials

Type III portland cement with a specific gravity of 3.15 and a Blaine fineness of 493 m2/kg was supplied by Lehigh Cement Company LLC. Undensified silica fume from Norchem with a SiO2 content of 95.7% and a specific gravity of 2.24, and Micron3 ultra fine fly ash from Boral Resources LLC with a median particle size of 2 to

4 micron and a specific gravity of 2.69 were used in this study to modify the matrix of cement binder. The chemical and mineral compositions of the cement, silica fume and fly ash are summarized in Figure 1. Masonry sand was used as aggregate for the UHPS. The particle size distributions (PSDs) of cement, silica fume, fly ash and masonry sand are shown in Figure 3. The overall PSDs of the cement and silica fume are relatively similar, but silica fume shows a higher fraction of particles with a diameter smaller than 3 m. The ultra-fine fly ash exhibited a relatively narrow PSD ranging between 0.8 m and 8 m. The median particle sizes (d50) of cement, silica fume, fly ash and masonry sand are 12.64 m, 17.89 m, 2.81 m and 398.83 m, respectively. Brass coated steel microfibers with a diameter of 0.008 in. (0.2 mm), a length of 0.51 in. (13 mm) and an average tensile strength of 421 ksi (2900 MPa) were used to as reinforcement in UHPC. An Optimum 380 high range water reducing (HRWR) admixture was used to improve workability the concrete mix.

	Oxides	Type III Cement	Silica Fume	Fly Ash
Oxides components (%)	Si O ₂	19.01	95.67	50.29
	Al_2O_3	5.46	-	16.27
	Fe_2O_3	2.19	-	5.23
	CaO	61.97	-	11.11
	MgO	2.51	-	3.72
	SO_3	4.63	0.27	1.66
	CO_2	1.84	-	
	C ₃ S	54.74	-	-
	C_2S	13.22	-	-
Dhasa samananta (0/)	C_3A	10.77	-	-
Phase components (%)	C_4AF	6.66	-	-
	$C_3S + 4.75C_3A$	98	-	-
	Equivalent Alkalis	1	0.31	7.15

Figure 1. Chemical composition of Type III cement, silica fume and fly ash.

3.2 Mixture design

In this study, two groups of concrete were prepared with one group of plain concrete without fiber as control group and one group reinforced with micro-steel fibers. The design of UHPC utilizes an optimum particle packing density of the solid components to achieve low porosity and high compressive strength. In this project, the Modified Andersen-Andreassen Model was employed, ¹⁰ via EMMA software from ELKEM Silicon Product, to reach the particle packing optimization. This model uses a modified equation in Eq. (3).

$$P(D) = \frac{D^q - D_{\min}^q}{D_{\max}^q - D_{\min}^q} \tag{3}$$

where P(D) is the fraction of total solids smaller than diameter D.^{11,12} q is the distribution modulus, which varies between 0.22 and 0.25.^{13,14} D_{\min}^q and D_{\max}^q are the minimum and the maximum diameters with distribution q, respectively. Based on the maximum and minimum size of the solid particles and a q value of 0.25, an ideal distribution curve was generated in EMMA (the red curve in Figure 3). After importing gradations for the cement, silica fume, fly ash and masonry sand into EMMA, adjustments of contents of the solid components were made until the PSD (the blue curve in Figure 3) of the mix matches the ideal packing curve. Based on this particle packing optimization, a binder consisted of 62% cement, 30% silica fume and 8% fly ash by weight

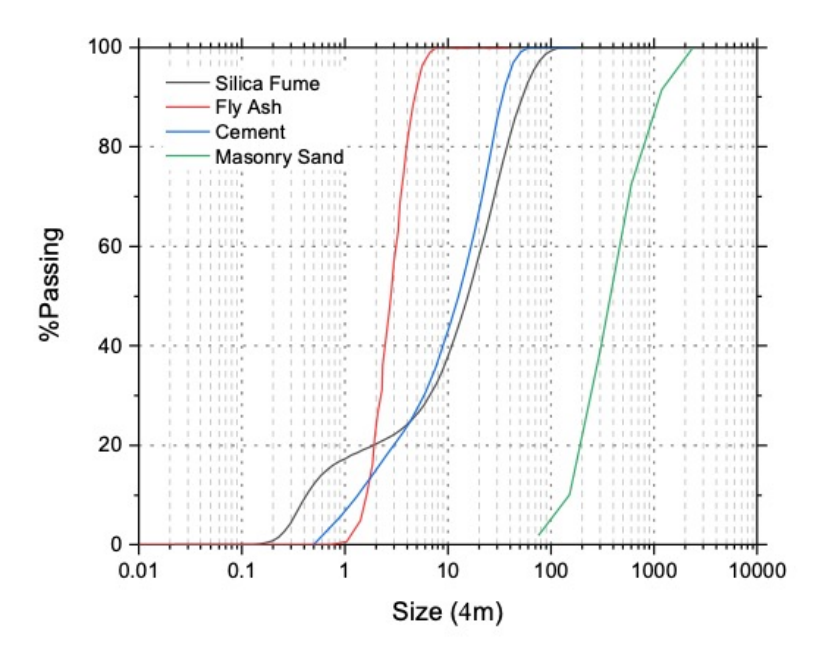


Figure 2. Particle size distribution of different materials.

was designed in this study. A fix w/b ratio of 0.19, a binder to sand ratio of 1.04 by weight, and a fiber volume fraction of 2% were employed for the UHPC mixture. A HRWR amount of 65 lb/yd3 was determined by making iterative trial mixes and obtaining a slum ranging between 8-10 in. The materials and mixture proportions of the UHPC are summarized in Figure 4.

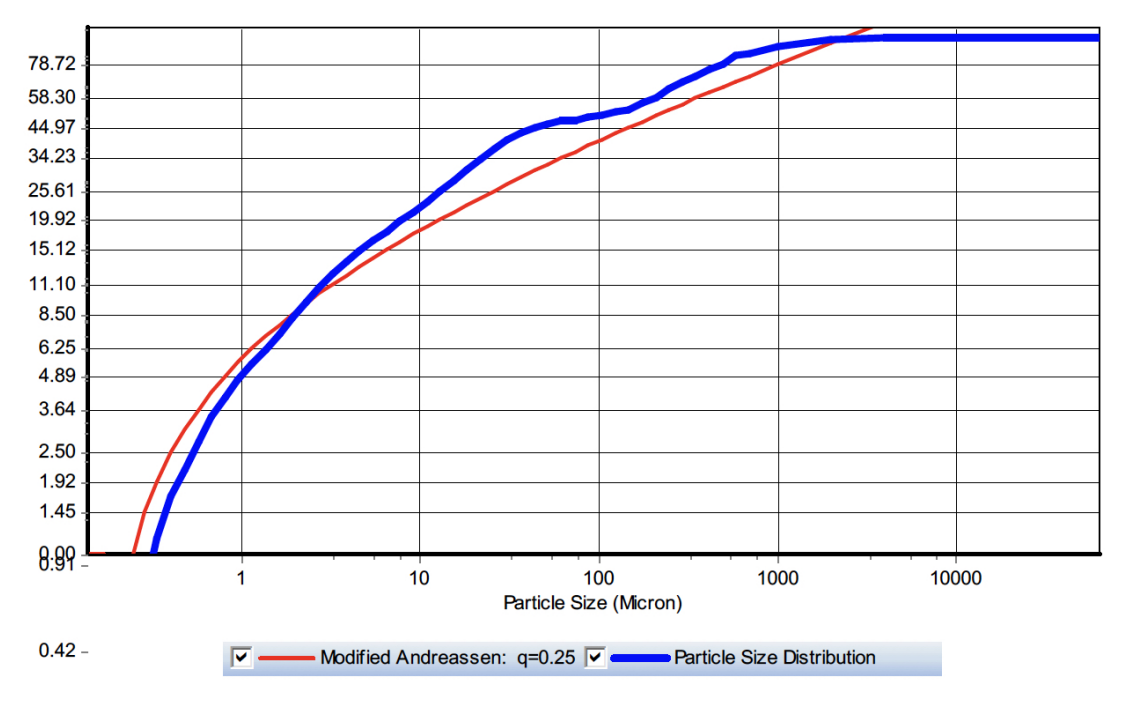


Figure 3. Particle size distribution of UHPC according to EMMA.

Material	Plain UHPC mixture (lb/yd³)	UHPC with fiber	
Cement	1264.2	1264.2	
Silica Fume	606.8	606.8	
Fly Ash	168.6	168.6	
Masonry Sand	2123.8	2123.8	
Water	387.5	387.5	
Superplasticizer	65	65	
Steel Microfiber	-	2% by volume	

Figure 4. Materials and mixture proportions of UHPC.

3.3 Mixing, casting and curing

According to ASTM C1856, the following mixing procedure was employed to obtain uniform mix with desirable flowability. A Gilson concrete mixer was used to mix the entire quantity of UHPC followed by shear mixing. The sand, silica fume and fly ash was dry mixed for 2 minutes. Cement was then added and mixed for 1 minute. Next, the water was added and mixed for 1 minute followed by the addition of HRWR and a 10 minutes mixing until a uniform mixture is obtained. For the group of steel fibers, the fibers were mixed following the addition of cement. The cylinder molds were filled in a single layer with the fresh UHPC followed by 25 times tamping to ensure proper consolidation. For each group, nine 3 in. by 6 in. cylinders and two 4 in. by 8 in. cylinders were cast. The specimens were demolded after 24 hours and air dried under a temperature of 25 ± 1 .C and relative humidity of $30\pm1\%$ throughout the curing period.

3.4 Testing methods

The workability of the plain and fiber reinforced UHPC was measured using both upright and inverted slump cone according to ASTM C143¹⁵ and ASTM C995.¹⁶ The initial autogenous shrinkage of both groups was measured using a shrinkage cone, which performs contactless high-resolution monitoring using a laser beam. The measurement was started immediately after mixing and continued up to 96 hours.

The permeability of the plain and fiber reinforced UHPC was determined indirectly by measuring the electrical bulk resistivity of 4 in. by 8 in. cylinders at a frequency of 1 kHz using a RCON device developed by Giatec. Before the measurement, the cylinders were first cured in lime water at 25 ± 1 .C for 2 days, then vacuum saturated in a simulated concrete pore solution for 3 hours followed by a 72-hour soaking. Two repetitions were employed for the bulk resistivity test. The bulk resistivity (ρ) was calculated using Eq. (4),

$$\rho = R \frac{A}{L} \tag{4}$$

where R= the bulk resistance, A= cross-sectional area and L= length of the cylindrical specimen. Compressive strength tests were conducted on 3 in. by 6 in. cylinders according to ASTM C39¹⁷ on a PILOT automatic compression tester at a uniform loading rate of 200 lbf/sec. Three repetitions were considered for the compression test.

3.5 Laboratory SAR imaging

Two groups of concrete were scanned by a laboratory 10-GHz SAR (synthetic aperture radar) imaging system with a 1.5-GHz bandwidth. This continuous wave imaging radar (CWIR) system was used along with an anechoic chamber in the Electromagnetic Remote Sensing Laboratory at UMass Lowell. A two-dimensional (2-D) positioner was utilized to move the CWIR system in the stripmap SAR imaging mode. Figure 5 shows the SAR imaging system and the anechoic chamber with a 2-D positioner.



Figure 5. Exterior of the anechoic chamber for laboratory SAR imaging

4. RESULTS AND DISCUSSION

4.1 Fresh properties

The slump of the plain concrete without fibers was measured to be 9.5 in. and 10.5 in. for the upright and inverted slump cone tests, respectively, while for the fiber reinforced UHPC the slump values were found to be 10.25 in. and 10.75 in. The improved workability of fiber reinforced UHPC may be caused by the ease of de-agglomeration of the particles in the presence of microsteel fibers, which facilitates the coating of particles by HRWR.

The evolution of autogenous shrinkage behavior and temperature inside both plain and fiber reinforced UHPC due to cement hydration heat are shown in Figures 6 and 7. From Figure 6, it can be found that the increasing rate of initial shrinkage during the first 6 hours was greater in fiber reinforced UHPC, which yielded a maximum shrinkage of 207.5 m after 10 hours. It is interesting to observe that the autogenous shrinkage of the UHPC with fiber reinforcement did not further increase with increasing time. However, even exhibited a lower shrinkage during the early age, a continuous increase of autogenous shrinkage was yielded by the plain concrete without fibers, which became higher than that of the reinforced group after 63 hours. This indicates the positive role of steel fibers in restricting volume change of the concrete admixture after its setting and hardening.

Similar with the development of shrinkage, the temperature also exhibited a rapid increase in the first 6 hours of casting due to the hydration of cement and pozzolanic reactions with the mineral admixtures. The peaks of the temperature correspond well with the peaks of the shrinkage behavior. During the first 5 hours, the plain group exhibited a higher increasing rate than the group with fibers, while the highest temperature was yielded by the fiber group, which is in good agreement of flowability and shrinkage results. Again, after 40 hours, a higher internal temperature was observed from the plain group. Short-term compressive strength of two groups of

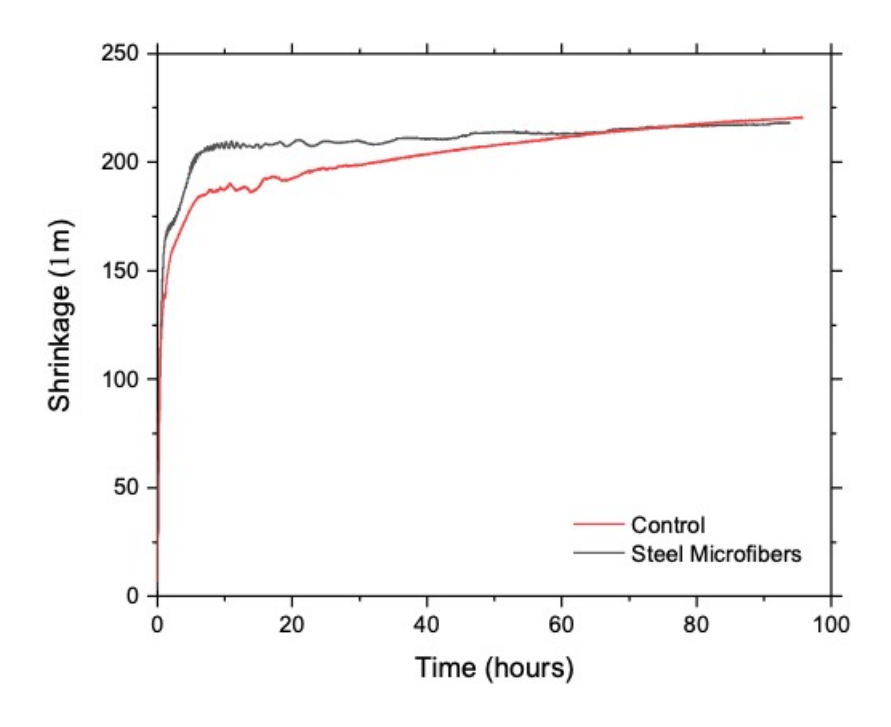


Figure 6. Evolution of autogenous shrinkage behavior

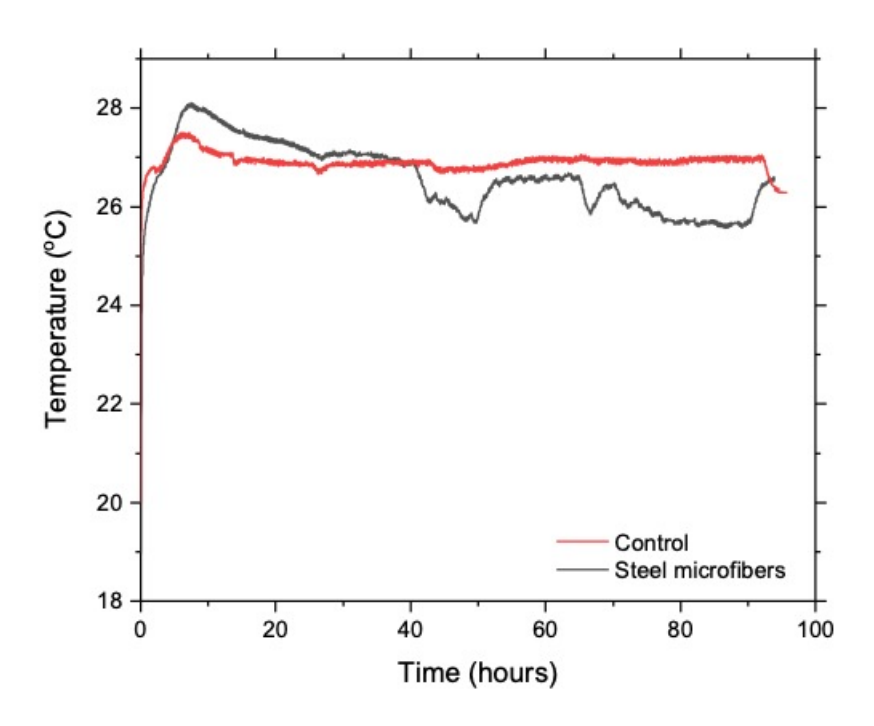


Figure 7. Temperature inside both plain and fiber reinforced UHPC

UHPC specimens was obtained by using a MTS (Material Testing System) machine in the Concrete Laboratory in the Department of Civil and Environmental Engineering at UMass Lowell. The result is shown in Figure 8. In Figure 8, each data point represents the average compressive strength of three specimens. It is clear that the overall growth of compressive strength of UHPC specimens is shown in Figure 8. The average compressive strength of Group 2 specimens at the age of Day 7 appears to be greater than the one of Group 1 specimens (control).

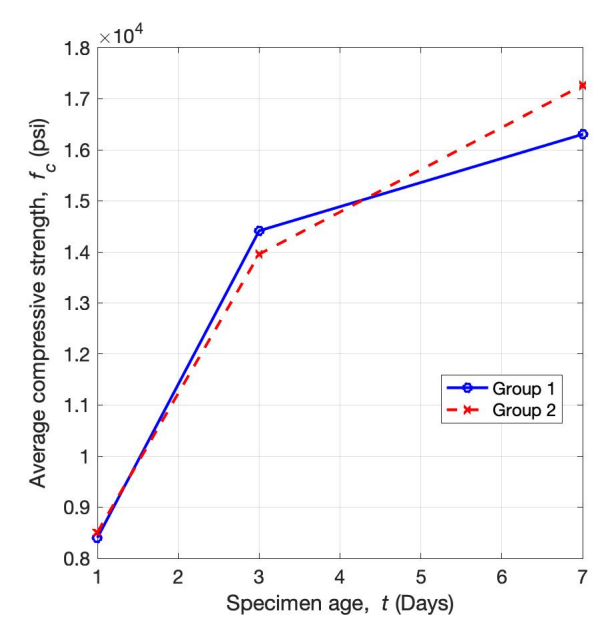


Figure 8. Average compressive strength of UHPC specimens

4.2 SAR images

SAR images of Group 1 specimens on Days 1, 3 and 7 are shown in Figures 9 \sim 11. Group 2 images are shown in Figures 12 \sim 14. Correlation between the short term compressive f_c and the maximum SAR amplitude I_{max} is illustrated in Figure 15, while the correlation between f_c and I_{int} is provided in Figure 16. From Figures 15 and 16, we have found that both I_{max} and I_{int} show very good correlation with f_c . This is because of the reduction of moisture content in UHPC over time, leading to the reduction of effective dielectric constant and loss factor of UHPC specimens.

5. CONCLUSION

This paper presents our experimental work on i) the use of the Andersen-Andreassen model to attain optimal particle packing density in the design of UHPC (ultra high performance concrete) and ii) the use of non-contact synthetic aperture radar (SAR) imaging technique for characterizing the short-term strength of plain UHPC and fiber-reinforced UHPC specimens. The fresh and hardened properties of the plain UHPC and fiber-reinforced UHPC were evaluated. From our imaging result, it is found that SAR images can reveal the subsurface profile of UHPC specimens. Other conclusions can be drawn and listed in the following:

1. The slump of fresh concrete measured via both upright and inverted slump cone tests showed that the UHPC reinforced with 2 vol.% micro-steel fibers had a higher slump of 10.25 in. and 10.75 in. when compared to plain UHPC, which exhibited slumps of 9.5 in. and 10.5 in. in the two tests, respectively. This finding indicates the positive role of the micro-steel fibers in mitigating agglomeration of the ultra-fine particles during UHPC mixing, which improves the uniform distribution of HRWR at low water to cement ratio.

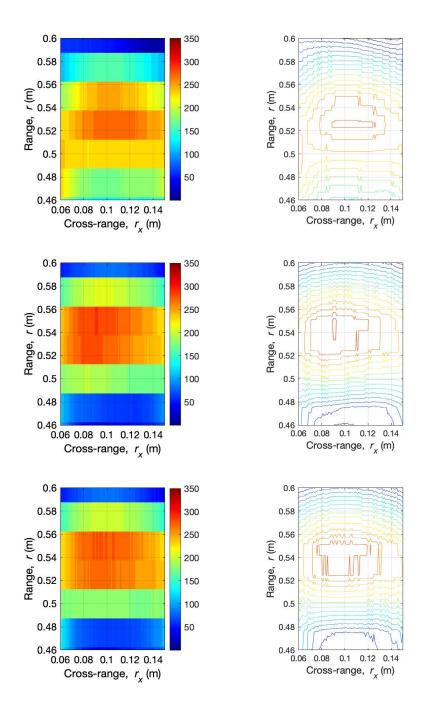


Figure 9. SAR images of Group 1 UHPC specimens on Day 1 $\,$

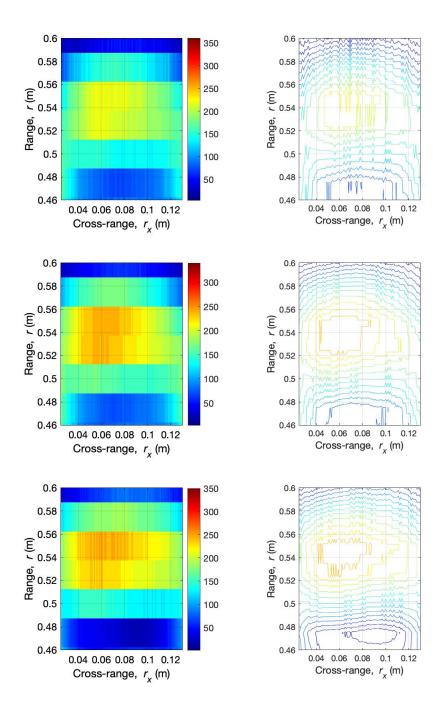


Figure 10. SAR images of Group 1 UHPC specimens on Day 3 $\,$

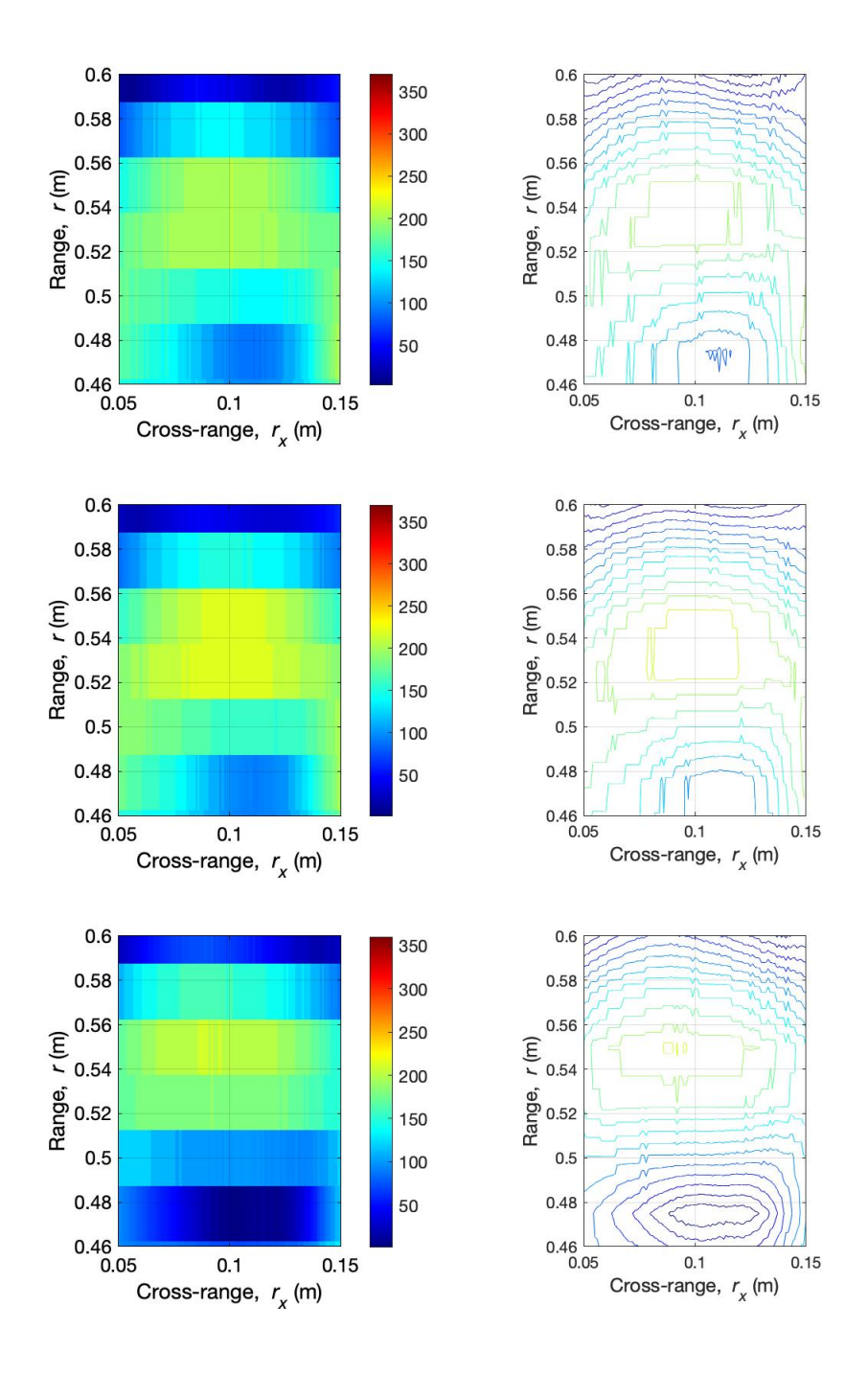


Figure 11. SAR images of Group 1 UHPC specimens on Day 7 $\,$

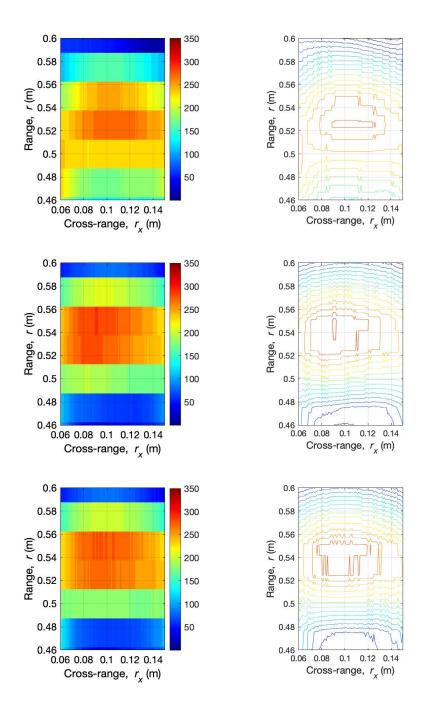


Figure 12. SAR images of Group 2 UHPC specimens on Day 1 $\,$

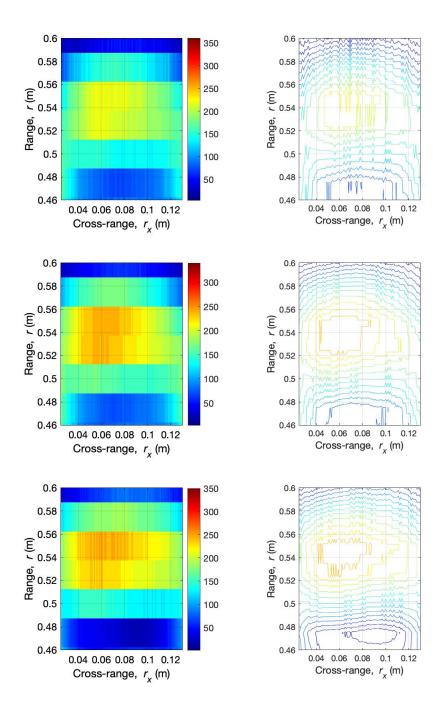


Figure 13. SAR images of Group 2 UHPC specimens on Day 3 $\,$

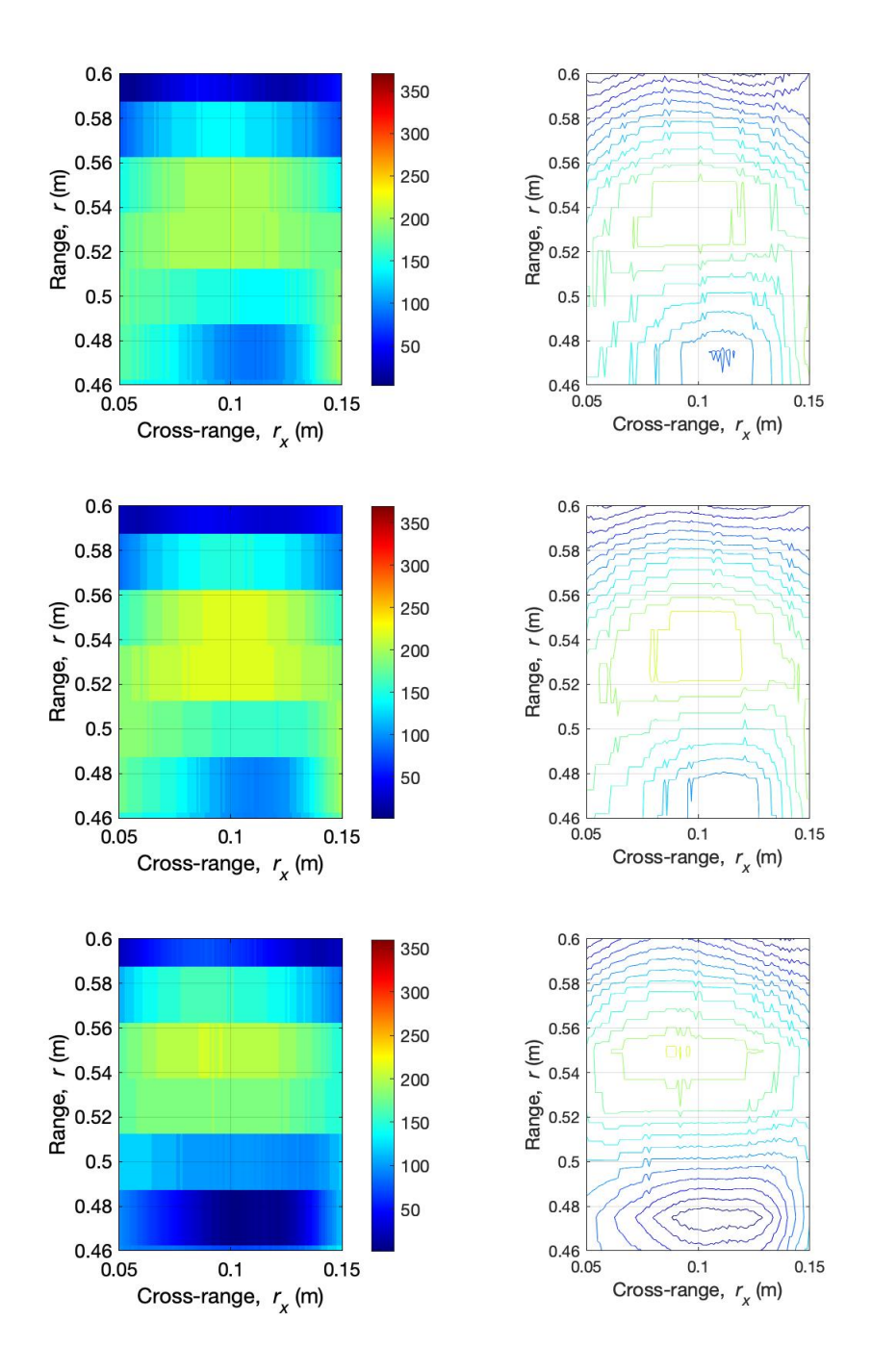


Figure 14. SAR images of Group 2 UHPC specimens on Day 7 $\,$

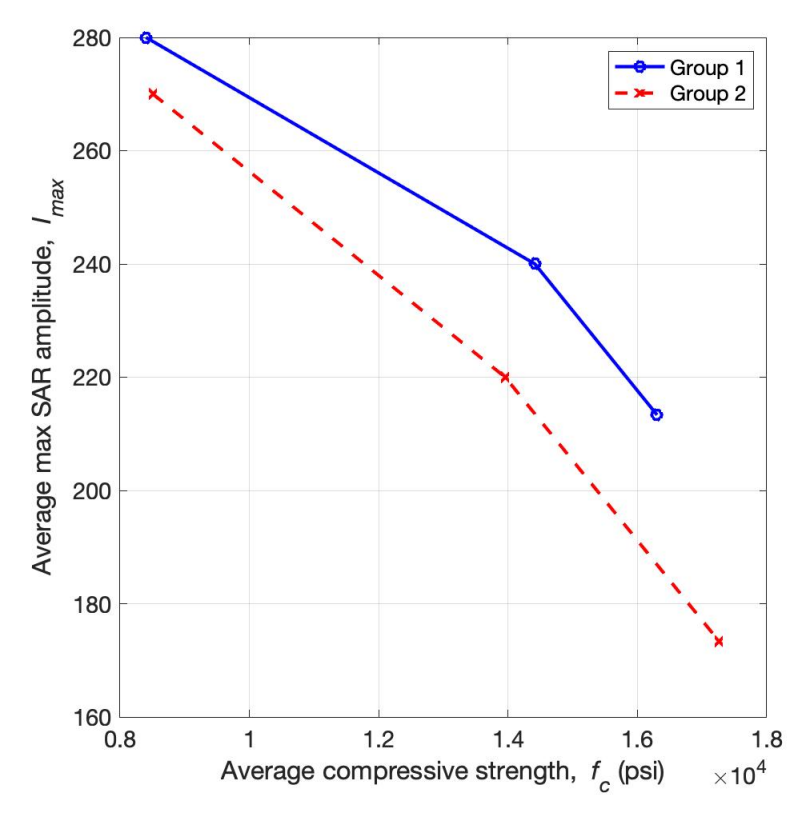


Figure 15. Correlation between f_c and I_{max}

- 2. The rate of autogenous shrinkage of the fiber-reinforced UHPC was higher than the plain group in the first 6 hours, after which it became constant, whereas the plain UHPC showed a continuously increased shrinkage and exceeded the fiber-reinforced UHPC after 63 hours. This difference indicates the contribution of steel fibers in restricting the volume change of the concrete admixture after hardening.
- 3. The use of Type III portland cement, silica fume, and ultra-fine fly ash enables a 1-day strength of 8.40 and 8.51 ksi in the pain and fiber-reinforced UHPCs, respectively. After 3 days, the two groups showed strength increases by 71.5% and 64%, respectively. 7-day strengths of 16.86 ksi and 16.81 ksi were yielded. In this study, it was observed that the influence of steel fibers on UHPC strength is negligible as the two groups yielded similar strength at all the three testing ages with a difference of less than 3.2%.
- 4. The bulk electrical resistivity and resistance of the plain UHPC were measured to be about 11 times that of UHPC reinforced with micro-steel fibers. However, in this study, the higher bulk resistance of the plain concrete group does not guarantee a lower permeability as in the fiber reinforced specimens the current might be conducted via the steel fibers in addition to pore solutions. Correspondingly, a higher deviation of bulk electrical resistivity was observed in the fiber-reinforced group due to the dependence of resistance on the distribution and connection of the fibers.
- 5. Both maximum SAR amplitude (I_{max}) and integrated SAR amplitude (I_{int}) can be used to estimate the compressive strength of UHPC specimens. The increase of compressive strength in UHPC specimens leads to the decrease of both maximum SAR amplitude (I_{max}) and integrated SAR amplitude (I_{int}) .

6. ACKNOWLEDGMENT

The authors want to thank the U.S. Department of Transportation (DOT) for partially supporting this research through a UTC (University Transportation Center) TIDC (Transportation Infrastructure Durability Center)

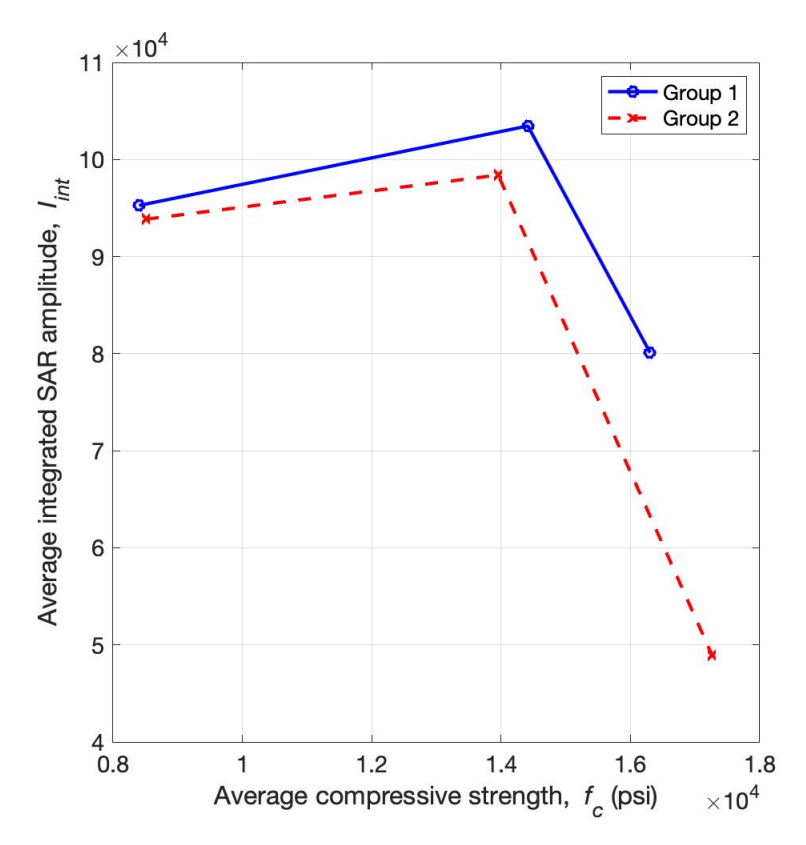


Figure 16. Correlation between f_c and I_{int}

project, including Project 1.4 "Electromagnetic Detection and Identification of Concrete Cracking in Highway Bridges" (Principal Investigator: T. Yu) and Project C3 "Condition Assessment of Corroded Prestressed Concrete Girders" (PI: T. Yu), both at UMass Lowell. We also like to express our gratitude to the National Science Foundation (NSF) for partially supporting this research through a CMMI (Civil, Mechanical, and Manufacturing Innovation) Award No. 1935799 "NanoEngineered Concrete Internal Conditioning for Targeted Suppression of Alkali-Silica Reaction" (PI: J. Wei).

7. DISCLAIMER

The contents of the research presented at this conference/document/presentation (select the appropriate content type) reflect the views of the researchers, who are responsible for the facts and the accuracy of the information presented. The findings presented in this (select the appropriate content type) conference/document/presentation are disseminated in the interest of information exchange. The research presented in this (select the appropriate content type) conference/document/presentation is funded, partially or entirely, by a grant from the U.S. Department of Transportation University Transportation Centers Program. However, the U.S. Government assumes no liability for the contents or use thereof.

REFERENCES

- [1] Wang, Z., Zeng, Q., Wang, L., Yao, Y., and Li, K., "Effect of moisture content on freeze-thaw behavior of cement paste by electrical resistance measurements," Journal of materials science 49(12), 4305–4314 (2014).
- [2] Zeng, Q., Fen-Chong, T., Dangla, P., and Li, K., "A study of freezing behavior of cementitious materials by poromechanical approach," International Journal of Solids and Structures 48(22-23), 3267–3273 (2011).
- [3] Cai, H. and Liu, X., "Freeze-thaw durability of concrete: ice formation process in pores," Cement and concrete research 28(9), 1281–1287 (1998).

- [4] Gonzalez, J., Lopez, W., and Rodriguez, P., "Effects of moisture availability on corrosion kinetics of steel embedded in concrete," Corrosion 49(12), 1004–1010 (1993).
- [5] Alzeyadi, A. and Yu, T., "Characterization of the range effect in synthetic aperture radar images of concrete specimens for width estimation," in [Nondestructive Characterization and Monitoring of Advanced Materials, Aerospace, Civil Infrastructure, and Transportation XII], 10599, 1059916, International Society for Optics and Photonics (2018).
- [6] Alzeyadi, A., Hu, J., and Yu, T., "Detecting underground metallic objects of different sizes using synthetic aperture radar," in [Sensors and Smart Structures Technologies for Civil, Mechanical, and Aerospace Systems 2019], 10970, 109702W, International Society for Optics and Photonics (2019).
- [7] Alzeyadi, A., Hu, J., and Yu, T., "Electromagnetic sensing of a subsurface metallic object at different depths," in [Nondestructive Characterization and Monitoring of Advanced Materials, Aerospace, Civil Infrastructure, and Transportation XIII], 10971, 1097105, International Society for Optics and Photonics (2019).
- [8] Kong, J., "Electromagnetic wave theory," EMW Publishing, Cambridge, MA (2000).
- [9] Yu, T.-Y., "Distant damage-assessment method for multilayer composite systems using electromagnetic waves," Journal of Engineering Mechanics 137(8), 547–560 (2011).
- [10] Andreasen, A., "ber die beziehung zwischen kornabstufung und zwischenraum in produkten aus losen krnern (mit einigen experimenten," Kolloid-Zeitschrift 50(3), 217–228 (1930).
- [11] Funk, J. and Dinger, D., "Predictive process control of crowded particulate suspensions: applied to ceramic manufacturing," Springer Science & Business Media (2013).
- [12] Brouwers, H., "Particle-size distribution and packing fraction of geometric random packings," Physical Review E 74(3), 031309 (2006).
- [13] Brouwers, H. and Radix, H., "Self-compacting concrete: theoretical and experimental study," Cement and Concrete Research 35(11), 2116–2136 (2005).
- [14] Hunger, M., "An integral design concept for ecological self-compacting concrete," Eindhoven University of Technology, Friedrichroda, Germany (2020).
- [15] ASTM-C143/C143M-20, "Standard test method for slump of hydraulic-cement concrete," ASTM International (2020).
- [16] ASTM-C995-01, "Standard test method for time of flow of fiber-reinforced concrete through inverted slump cone," ASTM International (2001).
- [17] ASTM-C39/C39M-20, "Standard test method for compressive strength of cylindrical concrete specimens," ASTM International (2020).